Seismic constraints on mantle flow and topography of the 660-km discontinuity: evidence for whole-mantle convection

Jason Phipps Morgan & Peter M. Shearer

Institute of Geophysics and Planetary Physics, University of California at San Diego, La Jolla, California 92093-0225, USA

Recent seismic models of three-dimensional mantle structure and topography on the transition-zone seismic discontinuities permit the direct evaluation of the buoyancy forces that drive large-scale mantle flow. This buoyancy distribution, coupled with radial viscosity models that are consistent with the observed geoid, predicts flow patterns with significant vertical flow through the 660-km phase boundary. The observed topography on the 660-km discontinuity acts to inhibit convection across the boundary, but is two to four times too small to prevent whole-mantle convection.

A FUNDAMENTAL issue in mantle convection is whether large-scale mantle flow is stratified by changes in mineral phase or bulk chemistry across the seismic discontinuity at 660 km[1-4]. This question has major implications for the potential mass and heat transfer throughout the mantle which strongly affect its chemical and thermal evolution[5]. Seismic imaging of subducting slabs has not resolved this issue, with some studies indicating slab penetration below the 660-km discontinuity[6,7], whereas others have found horizontal seismic velocity anomalies in some areas that suggest the slabs are deflected by the interface[8,9]. This debate has recently been reinvigorated by three-dimensional numerical experiments of mantle convection that include the effects of a phase change at 660 km, experiments that predict the possibility of significant amounts of flow stratification due to the negative Clapeyron slope of this phase transition[10-13], and an analysis that finds no change in the pattern of three-dimensional seismic velocity structure near 660-km depths as would be expected for layered convection[14].

Here we present a new approach to this problem. We use seismic tomographic maps of three-dimensional mantle velocity structure[15-18] and maps of the topography on the 410- and 660-km discontinuities[19,20] to infer directly the density distribution that drives large-scale mantle flow (the flow is caused by the buoyancy forces that arise from lateral density gradients). We explore the effects of this density distribution on mantle flow for several plausible radial viscosity structures[21,22] that have been proposed to fit the observed geoid, given the seismically inferred densities. The resulting vertical flow pattern for each viscosity model shows directly the amount of vertical mass transfer across the 660-km boundary as well as flow rates at other mantle depths. If mantle flow is layered as sketched in Fig. 1, the mean radial flux should show a strong reduction near 660-km depths[11]. In fact we see no apparent cusp at any depth in the curves of radial flux against depth, implying a coherent low-order pattern of whole-mantle flow. The observed topography on the 660-km discontinuity acts to oppose convection but is too small to prevent vertical flow. These results do not depend on the assumed Clapeyron slope of the 660-km phase change, and are robust with respect to reasonable variations in mantle viscosities and the viscosity-to-density scaling relationship.

Seismic models of 3-D mantle structure

Recent tomographic models of mantle shear-wave velocities now provide good global-scale information on the mantle density structure. Here we use two of these recent models, SH8WM13 (refs 17, 18) and SH10c (ref. 15) which, though based on mostly different data, show generally good agreement between their velocity structures. These seismic inversions recover a three-dimensional image of aspherical variations in seismic shear velocity β. Converting these velocity perturbations to aspherical density variations requires some assumptions. In regions where thermal effects are dominant (that is, compositional effects are small, see below), $\delta\beta$ is typically less than $\pm 2\%$ of the mean shear-wave velocity, and can be related to aspherical density variations by the linear approximation at constant pressure $\delta\rho = (\partial\rho/\partial\beta)_P \delta\beta$. The primary uncertainty is to what extent an increase in pressure reduces $(\partial\rho/\partial\beta)_P$. Laboratory measurements and seismic observations of slab anomalies[7] suggest that $(\partial \ln \rho/\partial \ln \beta)_P \approx 0.4$, with little depth dependence in the upper mantle. Although recent laboratory measurements predict $(\partial \ln \rho/\partial \ln \beta)_P$ to be relatively pressure-insensitive, Debye-Grüneisen theory suggests that it may decrease substantially with increasing pressure[23], and several models[21,24] have incorporated this assumption in determining radial viscosity models that fit the observed geoid with a seismically inferred density structure, using values of $(\partial \ln \rho/\partial \ln \beta)_P$ that vary from ~0.2–0.4 at upper mantle/transition-zone depths to ~0.1 in the lower mantle. Here we will explore the mantle flow predicted by two different viscosity models, one of which assumes that $(\partial \ln \rho/\partial \ln \beta)_P \approx 0.4$ throughout the mantle, whereas the other assumes that $(\partial \ln \rho/\partial \ln \beta)_P$ decreases from 0.2 in the upper mantle to 0.1 in the lower mantle (see Fig. 2). For consistency, we always use the velocity–density scaling appropriate for each model.

Topography on the 660-km discontinuity

The remaining mass anomalies that can drive mantle flow are due to vertical deflections of internal density discontinuities associated with chemical or phase traditions. Mineral physics experiments indicate that the 410-km discontinuity is caused mainly by the phase change between α- and β-olivine, and the 660-km discontinuity is mainly due to the transformation γ-spinel → perovskite + magnesiowüstite. The 410-km phase change is found to be an exothermic reaction with a positive Clapeyron slope (dP/dT) which should cause the discontinuity to move up in response to reduced temperatures. In contrast, the 660-km phase change is an endothermic reaction with a negative Clapeyron slope and should move down in colder regions. The 660-km discontinuity will tend to resist the penetration of both cold descending material or hot ascending material because the phase boundary is perturbed in the direction of flow and the restoring force induced by the density perturbation will oppose this flow. The situation is reversed for the 410-km discontinuity in which

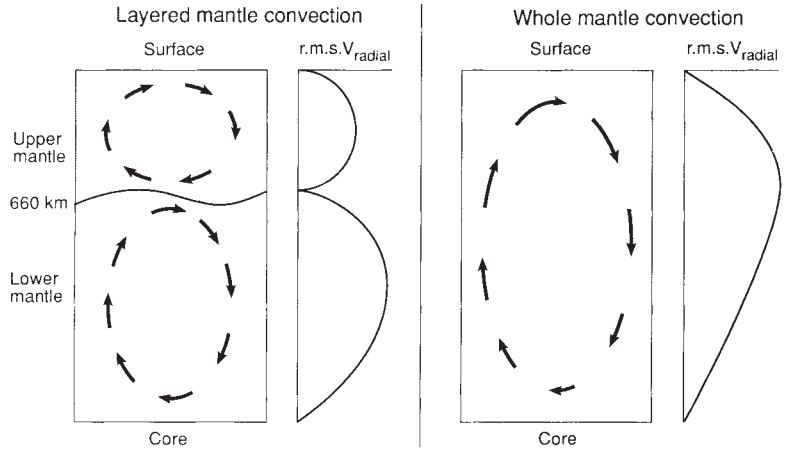

FIG. 1 Pattern of radial mantle flow implied in layered- and whole-mantle convection patterns. The radial flux across the 660-km discontinuity is a strong discriminant for the pattern of mantle convection.

the phase change acts to encourage thermally induced vertical flow.

The 660-km discontinuity is of most interest for this study because it acts to oppose vertical flow and is the depth for the proposed layering between the upper and lower mantle. Seismic observations based on reflected and converted phases suggest that topography on the 660-km discontinuity is less than 30–40 km[25,26]; this topography has been mapped recently on the global scale required for our analyses using long-period reflections[19,20]. (If a Clapeyron slope based on laboratory measurements is assumed, then the amplitude of phase-boundary relief could potentially be inferred via the circuit lateral $\delta\beta \rightarrow$ lateral $\delta T \rightarrow$ vertical phase boundary perturbation. Here we avoid the uncertainties of this procedure by measuring 660-km topography directly from seismic observations of reflected phases.) Because of the density contrast at 660 km, this topography implies the existence of significant lateral density anomalies at the interface. These density perturbations do not follow the same velocity-to-density scaling as do the thermal buoyancy forces discussed above.

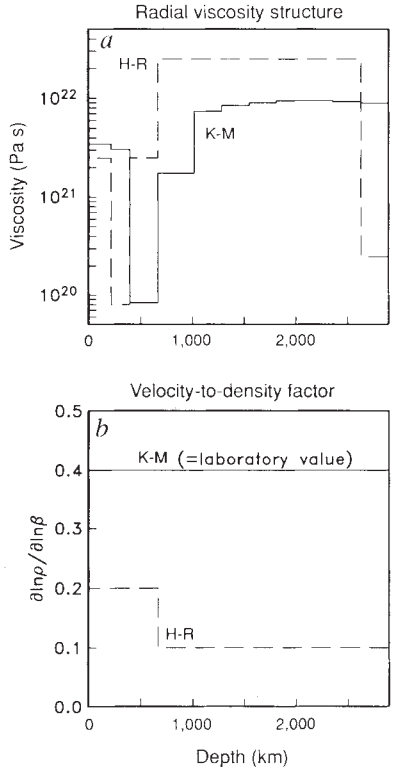

FIG. 2 *a*, Radial viscosity structure for two mantle viscosity models, H–R (Hager and Richards[21]) and K–M (King and Masters[22]), which successfully predict the observed geoid from buoyancy forces imaged by aspherical seismic velocity inversions. *b*, Corresponding velocity-to-density scaling required by each model to fit the observed geoid.

Relief on internal discontinuities will affect a tomographic inversion for aspherical velocity structure if these interfaces are assumed to be flat. We can, however, correct for this effect on our inferred densities by considering the velocity contrasts across the discontinuities. If an interface is perturbed by h in depth, a shear velocity anomaly occurs at the interface of height h and amplitude $\Delta\beta/\beta$, where $\Delta\beta$ is the discontinuity velocity contrast. Assuming $(\partial \ln \rho/\partial \ln \beta)_P = 0.4$ (appropriate for the upper mantle), the calculated density anomaly $(\Delta\rho/\rho)_{tomo} = 0.4\Delta\beta/\beta$. This typically severely underestimates the true $\Delta\rho$ at the interface. For example, at the 660-km discontinuity in PREM (ref. 27), $\Delta\beta/\beta = 6\%$, implying that $(\Delta\rho/\rho)^{660}_{tomo} = 2.4\%$, in contrast to the PREM $(\Delta\rho/\rho)^{660} = 9\%$. This is why it is necessary to include explicitly the density anomalies (due to boundary perturbations) in the buoyancy calculations, after first correcting for the small amount of the density anomaly which is expressed in the tomography results. Realistically, the limited vertical resolution in the tomographic inversion will cause the observed velocity anomalies due to discontinuity topography to be smeared out in shape and reduced in amplitude. The above correction is, however, still valid as our results do not depend very much on the exact depth and magnitude of the density anomalies, but only on their vertically integrated values which are better determined in tomographic inversions.

Geodynamic models of mantle flow

As discussed above, seismic methods can determine directly the large-scale aspherical mantle density structure that drives mantle flow. This density map, together with the observed geoid, can be inverted to give the radial viscosity structure of the mantle, one of the major geodynamic modelling achievements of the 1980s[21,22,24,28–33]. Recent geoid/tomography inversions crudely agree on the radial mantle viscosity structure[21,22,24,31]. In general, the upper mantle is about 10–30 times less viscous than the lower mantle, which has a viscosity of $\sim 10^{22}$ Pa s. Two recent models of radial mantle viscosity structure by Hager and Richards[21] (H–R model) and King and Masters[22] (K–M model) are shown in Fig. 2. The two models represent a range of plausible radial mantle viscosity structures. (Note that geoid fitting does not constrain the absolute magnitude of the mantle viscosity, only radial variation up to a multiplicative constant.) These models require different assumptions about velocity–density scaling

(Fig. 2*b*) to fit the peak-to-peak magnitude of the geoid; in particular, the H–R model requires that $(\partial \ln \rho / \partial \ln \beta)_P \approx 0.1$ in the lower mantle (similar models are determined by Forte *et al.*[24]), whereas the K–M model assumes that $(\partial \ln \rho / \partial \ln \beta)_P \approx 0.4$ throughout the whole mantle (similar models are determined by Ricard and Wuming[31]). For each viscosity model (and its corresponding velocity–density scaling) and the buoyancy distributions implied by each seismic model (and the seismic model's 'corrected' 660-km relief[20]), we solve for large-scale mantle flow assuming incompressible, self-gravitating viscous mantle flow[21].

Figure 3 shows the mean radial flow distribution that is predicted for the H–R and K–M models with the buoyancy forces implied by seismic models SH8WM13 and SH10c. Neither model shows a significant decrease in radial velocity near the 660-km discontinuity that would favour layered convection. The inclusion of the density anomalies due to the observed 660-km topography generally reduces velocities throughout the mantle (as would be expected if this barrier tends to oppose, but not stop downwelling at subduction zones), but still does not cause a local minimum in the r.m.s. velocity near the 660-km interface. Figure 4 shows the radial velocity distribution calculated from the H–R model, the SH8WM13 aspherical seismic velocity model, and Shearer's determination of 660-km relief[20] shown in Fig. 5*a*. The resulting mantle flow has an upwelling and downwelling pattern that differs little from mid-mantle to lower-mantle depths—that is, this flow structure is strongly coherent from one depth to another.

Some controversy exists regarding the radial resolution of the seismic velocity models, particularly in the vicinity of the 660-km discontinuity. Fortunately our results are not very sensitive to errors in the radial location of seismic velocity anomalies. For the low-order structure that dominates the seismic models, the flow near 660 km is driven by the effect of velocity perturbations averaged over 2,000 km or more in depth. There is a strong smoothing effect on the mantle flow from the buoyancy distribution that drives it: flow at a given depth responds in nearly the same manner to a density anomaly that is close in depth as it does to a similar density anomaly that is much deeper or shallower. (For example, the H–R response for flow at 660-km due to a degree-four mass anomaly at 2,000 km is only 35% less than that due to a mass anomaly at the 660-km interface itself. The response to lower-degree mass-anomalies is even less depth-sensitive.) Our predicted mantle flow pattern is determined largely by the vertically integrated effect of velocity anomalies in the mid-mantle. These large-scale radial averages of the tomography models are much better determined than the values at particular depths, because the seismic travel times used to derive the velocity models produce a similar smoothing effect.

To be sure that our method is capable of detecting a kink in the r.m.s. flow field if it existed, we created some hypothetical density distributions which predict such a kink even in the absence of any discontinuity topography. Our starting point is the calculated 660-km discontinuity topography (see below) required to stop flow across the discontinuity for the SH8WM13 model and H–R viscosity model. This introduces 9% density anomalies at 660 km, which are sufficient to counter the other buoyancy forces in the mantle to enforce layered convection. Thus, a model with intrinsic density anomalies (as opposed to boundary deflections) of this size at 660 km would also result in layered convection, and require no discontinuity topography. The predicted r.m.s. flow for this model is shown as the solid line in Fig. 3*b*, and contains a null point at 660 km. However, the low radial resolution of the seismic tomography will smear out a pronounced density anomaly right at 660 km, so we experimented to see how this would affect our results. The dashed line in Fig. 3*b* shows the r.m.s. flow predicted when the mass anomalies are uniformly smeared over 600 km; the dotted line shows

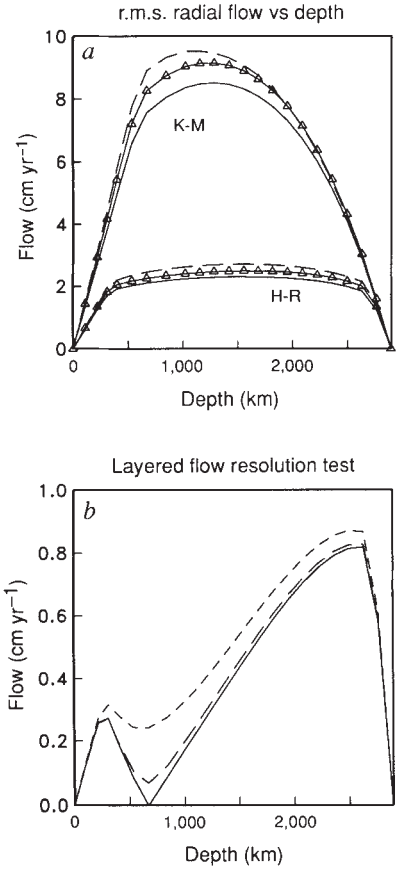

FIG. 3 *a*, R.m.s. radial mantle flow pattern with depth that is predicted by several density and viscosity hypotheses. The top three profiles are for the K–M model, and the bottom three are for the H–R model. For each model, the solid line is for the SH8WM13 density model, a PREM density jump at 660-km, and the map of 660-km relief[20] shown in Fig. 5. Triangles show radial flow patterns for buoyancy distributions that do not include the effects of the 660-km relief; these models have generally higher flow rates throughout the entire mantle. Dashed lines show models that include the effects of 660-km topography and the SH10c buoyancy distribution. All models show no hint of a significant reduction in vertical flow through the 660-km interface that would indicate layered mantle convection as sketched in Fig. 1. *b*, Results from a synthetic resolution test where, for the SH8WM13 density model and H–R viscosity model, the mass anomaly at 660 km needed for layered convection (shown in Fig. 5) is added to the SH8WM13 density field. The solid line shows the predicted r.m.s. radial flow when this additional mass anomaly is concentrated at 660 km, the dashed line shows the r.m.s. flow diagnostic when the mass anomaly is uniformly smeared over 600 km (from 360 to 960 km), and the dotted line shows the r.m.s. diagnostic when the mass anomaly is smeared over 1,200 km (from 100 to 1,300 km).

the result when the anomalies are uniformly smeared over 1,200 km. In each case there is a pronounced kink in the r.m.s. flow near 600 km. Most discussions of the vertical resolution of the tomography models suggest resolving lengths of 400 km or better, but even if the resolutions were as poor as 600–1,200 km, our method would still produce a kink in the r.m.s. flow for these models. In fact, these density distributions, when converted to S-velocity anomalies, predict travel-time residuals for vertically travelling S-waves of 5 s (K–M model) to 7 s (H–R model). These are big anomalies, which would be detected easily by seismic means.

The mantle flow rates predicted by the H–R model are large, ~4 cm yr^{-1}, and the K–M model predicts even larger vertical flow rates. Although lower-mantle horizontal flow rates are typically half as large as vertical flow rates, these speeds still seem relatively high: mean vertical flow rates of 4 cm yr^{-1} imply a cycle time of ~150 Myr to traverse the mantle. Although the geoid is insensitive to the absolute magnitude of the mantle viscosity, flow rates scale to the reciprocal of viscosity. Increasing all viscosities in the H–R model by a factor of two would still generate an upper-mantle viscosity structure that is consistent with glacial rebound constraints while cutting mean vertical flow speeds in half. Increasing all viscosities in the K–M model by a factor of six to ten would lead to comparable lower-mantle vertical flow rates of ~1–2 cm yr^{-1}. Note that scaling a mantle viscosity model by a constant factor does not change the shape, but only the absolute magnitude of the predicted flow field; our conclusions regarding whole-mantle versus layered-mantle convection are not affected.

Figure 5*a* shows the observed topography on the 660-km discontinuity[20] after correcting for the effects of lateral velocity variations in the mantle. Regional depressions are seen in the western Pacific, South America and the North Atlantic, with highs near Africa and Eurasia; peak-to-peak depth variations are about 32 km. Figure 5*b* and *c* shows the topography on the 660-km discontinuity that is needed for layered mantle convection assuming the SH8WM13 mantle heterogeneity model (similar relief structures are seen for the SH10c model). Although these patterns are similar in shape to the observed topography, the H–R model (Fig. 5*b*) requires peak-to-peak depth variations in the interface of about 65 km, whereas the K–M model (Fig. 5*c*) needs depth variations of 130 km. Thus, our results show that the observed topographic variations in the 660-km discontinuity are from two to four times too small to prevent whole-mantle convection.

Implications for mantle dynamics

The general correlation between the observed 660-km interface deflection and the flow pattern seen in Fig. 4 is to be expected. Subduction zones should represent regions where cold material is advected downwards, thereby depressing an endothermic phase boundary. In contrast, upwelling regions are likely to have elevated temperatures that raise the depth at which the phase transition takes place. This should also cause a correlation between the maps predicted to enforce layered flow and seismic observations of 660-km relief. Figure 5 shows that there is only rough spatial coherence between these patterns. Some of the differences between the patterns are probably due to inaccuracies in the topography model caused by gaps in spatial coverage[20], but in several regions the disagreement seems to be real. In particular, North Atlantic and Eurasia are prominent areas where these two pictures are anticorrelated. Note that these are regions where

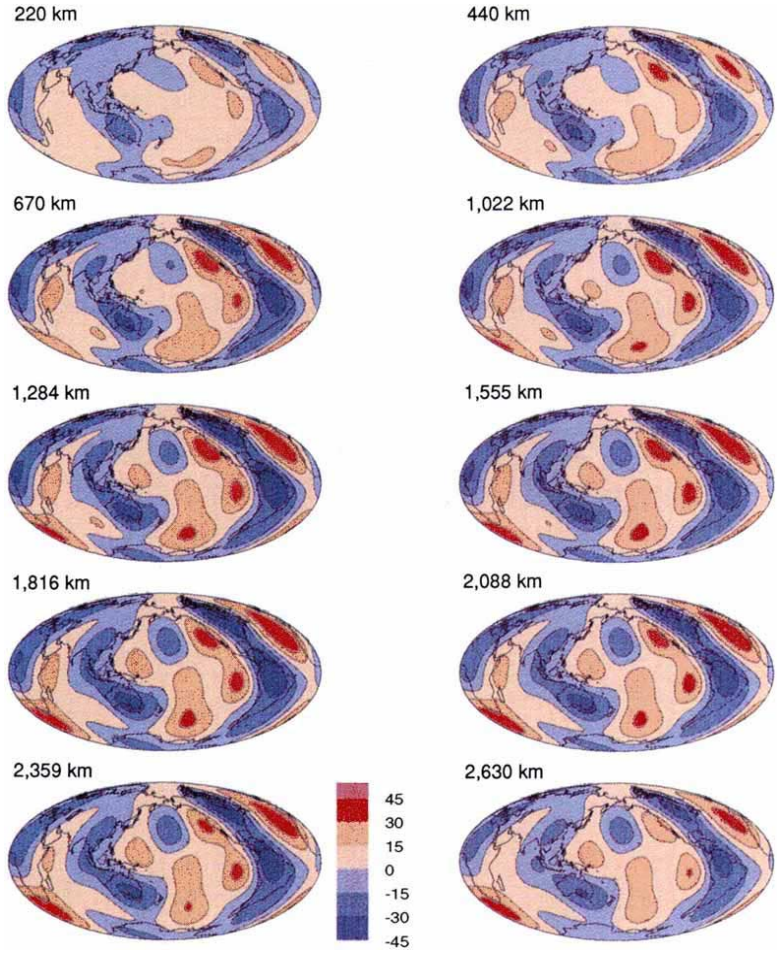

FIG. 4 Radial mantle velocity pattern predicted by the H–R viscosity structure, buoyancy forces due to 660-km topography with a PREM density jump, and the SH8WM13 buoyancy distribution. Vertical flow rates are shown at ten layers from upper-mantle to lower-mantle depths. Note the strong coherence between upper-mantle and lower-mantle centres of upwelling and downwelling; this flow pattern implies a top-to-bottom of large-scale mantle circulation. Velocity scale is in mm yr^{-1}.

active mantle flow may be relatively slow, so that the lateral temperature structure (which integrates a long previous flow history) is not in phase with the vertical flow pattern (which is a response to the current buoyancy distribution).

An advantage of our approach is that our results do not depend upon the assumed Clapeyron slope, γ_{660}, of the 660-km phase transition. Nevertheless, we can calculate an approximate value of γ_{660} from the seismic tomography and discontinuity topography observations. Velocity perturbations at 660 km in the three-dimensional mantle models are correlated approximately with the pattern of the topography seen in Fig. 5. The SH8WM13 model has peak-to-peak variations in shear velocity of 2.4% at 660 km, whereas the SH10c model has 3.7% variations. If we assume a scaling between shear velocity and temperature, $\partial\beta/\partial T$, that is consistent with laboratory measurements and seismic observations of slab anomalies[7,26], then an increase in shear velocity of 1% corresponds to a change in temperature of 100 °C. To fit the observed peak-to-peak topography of 32 km, γ_{660} ranges from −3.4 to −5.3 MPa per °C for the SH10c and SH8WM13 models. These numbers are in reasonable agreement with recent laboratory measurements[34] of the γ-spinel→perovskite+magnesiowüstite phase change which indicate $\gamma_{660} = -4 \pm 2$ MPa per °C. This is encouraging as the peak-to-peak amplitudes in the seismic models can be influenced by the degree of horizontal smoothing imposed during the inversion—the consistency between predicted and measured values of γ_{660} suggests that this is not a problem in our analysis.

Given that our results clearly indicate whole-mantle flow at $\gamma_{660} \approx -4$ MPa per °C, it is puzzling that recent numerical simulations of convection[10–12] suggest that layering or intermittent mixing can occur at values of γ_{660} between −2 and −4 MPa per °C (convection is inhibited more at steeper values of the Clapeyron slope because the discontinuity is perturbed more for a given temperature anomaly). Possible explanations for this discrepancy include temperature-dependent viscosity in the mantle and the large lateral scale of the velocity anomalies in the tomography studies. The numerical studies assume isoviscous, or simply layered, viscosity structures, whereas the actual mantle flow involves a temperature-dependent mantle rheology which can maintain much larger lateral temperature structure. Large lateral density anomalies will pass through the 660-km discontinuity more readily than small anomalies of the same amplitude, because it is more difficult for the material to be dispersed horizontally. Such a wavelength dependence in the vertical flow has been noted in numerical modelling experiments[12]. The very large horizontal scale of the anomalies seen in the tomographic images are a critical factor in our buoyancy calculations which implies whole-mantle convection. If the features were of much smaller wavelength then it is likely that layered convection could result.

Thus, it is important to consider the extent to which the lack of resolution in the seismic models is affecting our results. The models express velocity perturbations in spherical harmonics up to degrees eight to ten, limiting the horizontal resolution of heterogeneity to wavelengths of ~4,000 km or longer. But the spectrum of heterogeneity in the models is not flat; most of the power is contained in the first six harmonic degrees, and some seismic results indicate that heterogeneity may remain relatively weak out to degree 36 (~1,000 km wavelength)[35]. At even shorter scales, neither the global tomography nor the large-scale mantle flow models discussed here realistically images narrow rising plumes or subducting slabs; they are models only of the large-scale background mantle flow. Plumes will have a minor effect on the size of the background flow, the concentrated buoyancy force of a ~100 km diameter plume is relatively small compared

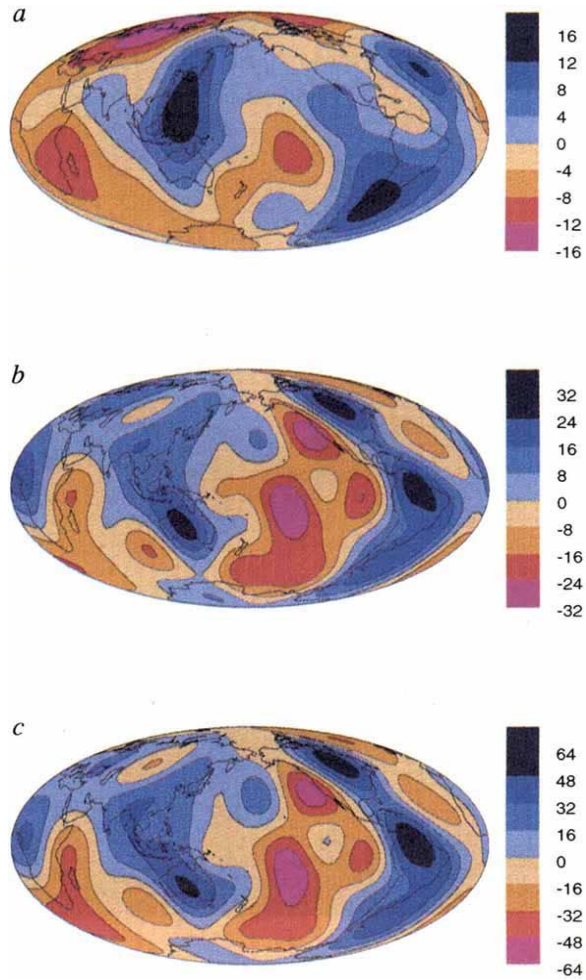

FIG. 5 *a*, Observed topography at the 660-km interface, calculated using the SH8WM13 model of aspherical seismic velocity structure (the topography calculated using the SH10c velocity model is quite similar). Positive relief corresponds to a deeper phase-boundary interface. *b*, 660-km relief needed for layered convection (no flow across the 660-km interface) for the H–R model and a PREM jump in density across the 660-km discontinuity (9% increase). This model predicts twice the peak-to-peak topography than is observed. *c*, 660-km relief needed for layered convection for the K–M model and a PREM jump in density across the 660-km discontinuity. This model predicts four times the peak-to-peak topography than is observed. The major reason for the increase relative to the H–R model is that the K–M model assumes a laboratory scaling of velocity to density in the lower mantle which is four times larger than the H–R value. Depth perturbations are contoured in km, with blue regions corresponding to depressions in the discontinuity.

with the regional buoyancy forces which are included in our calculations, and the regional heating from persistent plume concentrations is probably also incorporated. (For example, a 'hot region' in the South Central Pacific is a persistent feature at all depths in our aspherical density models. This region lies below a major cluster of surface hotspots.) Although the global tomography results do not resolve narrow subducting slabs, they do resolve a cold regional halo about major circum-Pacific subduction zones. If we are underestimating the negative buoyancy in the slabs, this missing buoyancy would act to enhance background downwelling near active subduction zones, implying that these results are a relatively conservative estimate of the forces driving background flow through the 660-km discontinuity.

Descending slabs represent an interesting combination of the factors of size and temperature-dependent viscosity. Their relatively small volume inhibits penetration through the 660-km discontinuity while their colder temperatures make them stronger and more likely to penetrate this discontinuity. This is because the slab will act as a stress guide for the negative buoyancy force above and below the phase transition. The trade-off between these effects may explain why seismic studies[6,9] indicate that in some areas slabs penetrate through the discontinuity, whereas in other regions the slabs are deflected by the discontinuity to form large pools of cold material in the transition zone behind the subduction zones (the results discussed here indicate that these regions also eventually sink through the discontinuity).

Validity of modelling assumptions

It is unlikely that a simple velocity–density scaling relationship based on temperature variations is valid throughout the mantle[36,37]. Instead, there probably exist compositional boundary layers near the surface and within the D″ region at the core–mantle boundary in which density cannot easily be predicted from velocity. To test this possibility, we repeated our flow calculation for the case in which buoyancy forces were removed from both the top 400 km and the bottom 300 km of the mantle, and found nearly the same flow across the 660-km discontinuity. Again, this emphasizes that it is the integrated effect of the velocity anomalies in the mid-mantle which are most important in determining the large-scale flow pattern.

Another potential weak spot in our mantle flow calculations is the assumed mantle viscosity models. Most of these models were derived to fit the observed geoid by assuming whole-mantle flow. Could alternative viscosity models exist that are consistent with layered-mantle flow? Attempts to produce such models have so far been unsuccessful in fitting the geoid[24], or have required a compositional boundary near 660 km with hundreds of kilometres of dynamic topography[21]. As we have discussed, such topography is precluded by seismic observations of discontinuity depths. Thus it seems improbable that a viscosity structure exists which could produce layered flow and remain compatible with gravity and seismic observations. An important next step in mantle viscosity calculations (based on fitting the geoid) will be to incorporate the observed 660-km topography as an additional constraint.

For the results discussed above we have assumed the PREM density contrast of about 9% at the 660-km discontinuity. A larger density contrast would cause the 660-km discontinuity to resist vertical flow more strongly for the same depth perturbation. Thus, whole-mantle convection could conceivably be prevented if $\Delta\rho_{660}$ were large enough. The required values of $\Delta\rho_{660}$ vary from 18% (H–R model) to 36% (K–M model). The PREM density contrast is, however, slightly larger than most other seismic estimates[26,38,39]; a value of 18% would be difficult, if not impossible, to reconcile with seismic data and mineral physics results for the 660-km phase change.

Our results show that current models of mantle velocity heterogeneity, discontinuity topography and radial viscosity structure strongly imply a whole-mantle pattern of circulation. This result seems to be robust with respect to considerable variations in these models, the velocity–density scaling relationship and the density jump across the 660-km discontinuity. But it should be possible to constrain our results better from improved seismic experiments and laboratory measurements in the near future. A critical challenge in future geodynamic modelling will be to find numerical models consistent with the observed pattern of mantle velocity and discontinuity perturbations. □

Received 31 March; accepted 10 September 1993.

1. Silver, P. G., Carlson, R. W. & Olson, P. *A. Rev. Earth planet. Sci.* **16,** 477–541 (1988).
2. Jeanloz, R. in *Mantle Convection: Plate Tectonics and Global Dynamics* (ed. Peltier, W. R.) 203–259 (Gordon & Breach, New York, 1989).
3. Jordan, T. H., Lerner-Lam, A. L. & Creager, K. C. in *Mantle Convection: Plate Tectonics and Global Dynamics* (ed. Peltier, W. R.) 98–201 (Gordon & Breach, New York, 1989).
4. Olson, P., Silver, P. G. & Carlson, R. W. *Nature* **344,** 209–215 (1990).
5. Wyllie, P. *Rev. Geophys.* **26,** 370–404 (1988).
6. Jordan, T. H. *J. Geophys.* **43,** 473–496 (1977).
7. Creager, K. C. & Jordan, T. H. *J. geophys. Res.* **91,** 3573–3580 (1986).
8. van der Hilst, R., Engdahl, R., Spakman, W. & Nolet, G. *Nature* **353,** 37–43 (1991).
9. Fukao, Y., Obayashi, M., Inoue, H. & Nenbai, M. *J. geophys. Res.* **97,** 4809–4822 (1992).
10. Machetel, P. & Weber, P. *Nature* **350,** 55–57 (1991).
11. Peltier, W. R. & Solheim, L. P. *Geophys. Res. Lett.* **19,** 321–324 (1992).
12. Tackley, P. J., Stevenson, D. J., Glatzmeier, G. A. & Schubert, G. *Nature* **361,** 699–704 (1993).
13. Honda, S., Yuen, D. A., Balachandar, S. & Reuteler, D. *Science* **259,** 1308–1311 (1993).
14. Jordan, T. H., Puster, P., Glatzmaier, G. A. & Tackley, P. J. *Science* (in the press).
15. Masters, T. G., Bolton, H. & Shearer, P. *EOS* **73,** 201 (1992).
16. Masters, G. & Bolton, H. *J. geophys. Res.* (in the press).
17. Su, W.-J., Woodward, R. L. & Dziewonski, A. M. *EOS* **73,** 201 (1992).
18. Woodward, R. L., Forte, A. M., Su, W.-J. & Dziewonski, A. M. *Geophysical Monograph* No. 74 89–109 (Am. Geophys. Un., Washington, DC, 1993).
19. Shearer, P. M. & Masters, T. G. *Nature* **355,** 791–796 (1992).
20. Shearer, P. M. *Geophys. Res. Int.* (in the press).
21. Hager, B. H. & Richards, M. A. *Phil. Trans. R. Soc.* A**328,** 309–327 (1989).
22. King, S. D. & Masters, G. *Geophys. Res. Lett.* **19,** 1551–1552 (1992).
23. Duffy, T. S. & Ahrens, T. J. *J. geophys. Res.* **97,** 4503–4520 (1992).
24. Forte, A. M., Dziewonski, A. M. & Woodward, R. L. *Geodynamic Ser.* (Am. Geophys. Un., Washington, DC, in the press).
25. Richards, M. A. & Wicks, C. W. *Geophys. J. Int.* **101,** 1–35 (1990).
26. Revenaugh, J. & Jordan, T. H. *J. geophys. Res.* **96,** 19763–19780 (1991).
27. Dziewonski, A. & Anderson, D. L. *Phys. Earth planet. Inter.* **25,** 297–356 (1981).
28. Richards, M. A. & Hager, B. H. *J. geophys. Res.* **89,** 5987–6002 (1984).
29. Ricard, Y., Fleitout, L. & Froidevaux, C. *Ann. Geophysicae* **2,** 267–286 (1984).
30. Hager, B. H., Clayton, R. W., Richards, M. A., Comer, R. P. & Dziewonski, A. M. *Nature* **313,** 541–545 (1985).
31. Ricard, Y. & Wuming, B. *Geophys. J. Int.* **105,** 561–571 (1991).
32. Forte, A. & Peltier, R. *J. geophys. Res.* **96,** 20131–20159 (1991).
33. Forte, A. M., Peltier, W. R. & Dziewonski, A. M. *Geophys. Res. Lett.* **18,** 1747–1750 (1991).
34. Ito, E., Akaogi, M., Topor, L. & Navrotsky, A. *Science* **249,** 1275–1278 (1990).
35. Su, W.-J. & Dziewonski, A. M. *Nature* **352,** 121–126 (1991).
36. Bolton, H. & Masters, G. *EOS* **73,** 403 (1992).
37. Hager, B. H., Grotzinger, J. P., Shapiro, S. S. & Panasyuk, S. V. *EOS* **74,** 298–299 (1993).
38. Gilbert, F. & Dziewonski, A. M. *Phil. Trans. R. Soc.* A**278,** 187–269 (1975).
39. Dziewonski, A. M., Hales, A. L. & Lapwood, E. R. *Phys. Earth planet. Int.* **10,** 12–48 (1975).

ACKNOWLEDGEMENTS. We thank G. Masters and S. King for discussions and advice regarding the models and subroutines used in this project. This work was inspired by R. Peltier who introduced the idea of using radial flux variations as a discriminant to test models versus layered mantle convection. This research was supported by the US National Science Foundation.